Disentangling Oxygen and Water Vapor Effects on Optoelectronic Properties of Monolayer Tungsten Disulfide

ARTICLE

Disentangling Oxygen and Water Vapor Effects on Optoelectronic Properties of Monolayer Tungsten Disulfide

Hanyu Zhang[a], Jeremy R. Dunklin[a], Obadiah G. Reid[a,b], Seok Joon Yun[c], Sanjini U. Nanayakkara[a], Young Hee Lee[c,d], Jeffrey L. Blackburn[a], and Elisa M. Miller[a]*

By understanding how the environmental composition impacts the optoelectronic properties of transition metal dichalcogenide monolayers, we demonstrate that simple photoluminescence (PL) measurements of tungsten disulfide (WS_2) monolayers can differentiate relative humidity environments. In this paper, we examine the PL and photoconductivity of chemical vapor deposition grown WS_2 monolayers under three carefully controlled environments: inert gas (N_2), dry air (O_2 in N_2), and humid nitrogen (H_2O vapor in N_2). The WS_2 PL is measured as a function of 532-nm laser power and exposure time and can be decomposed into the exciton, trion, and lower energy state(s) contributions. Under continuous illumination in either O_2 or H_2O vapor environment, we find dramatic (and reversible) increases in PL intensity relative to the PL in an inert environment. The PL bathochromically shifts in an O_2 environment and is dominated by increased trion emission and diminished exciton emission. In contrast, the WS_2 PL increase in a H_2O environment results from an overall increase in emission from all spectral components where the exciton contribution dominates. The drastic increases in PL are anticorrelated with corresponding decreases in photoconductivity, as measured by time-resolved microwave conductivity. The results suggest that both O_2 and H_2O react photochemically with the WS_2 monolayer surface, modifying the optoelectronic properties, but do so *via* distinct pathways. Thus, we use these optoelectronic differences to differentiate the amount of humidity in the air, which we show with 0%, 40%, and 80% relative humidity environments. This deeper understanding of how ambient conditions impact WS_2 monolayers enables novel humidity sensors as well as a better understanding of the correlation between TMDC surface chemistry, light emission, and photoconductivity. Moreover, these WS_2 measurements highlight the importance of considering the impact of the local environment on reported results.

Introduction

Transition metal dichalcogenides (TMDCs) — layered structures of MX_2 where M can be Mo or W (or other transition metal) and X = S, Se, or Te — have been investigated extensively due to the tunability of their optoelectronic properties from two-dimensional quantum confinement.[1–5] With their diverse properties (*e.g.*, high carrier mobilities, high absorption coefficients, and tuneable bandgaps), monolayer TMDCs can serve as field-effect transistors, optical sensors, photocatalysts, electrocatalysts, gas sensors, and carrier-transport layers in solar cells.[5–12] With this range of applications, it is critical to understand how the optoelectronic properties of monolayer

TMDCs are impacted by the environmental conditions during experimental measurements and/or device processing.[13–15] Among the many studies exploring the air sensitivity of 2D materials,[16,17] several studies have reported the optoelectronic properties of monolayer TMDCs affected by gas molecules in the environment, where TMDCs are serving as gas sensors, such as monolayer MoS_2 to detect NO_2, WS_2 monolayer to detect ammonia, WS_2 based all-fiber optic humidity sensor, and VS_2 nanosheets responding to relative humidity.[18–21]

The photoluminescence (PL) of TMDC monolayers, such as MoS_2 and WS_2, is strongly influenced by O_2 and/or H_2O.[3,22–31] Atmospheric O_2 and H_2O can significantly impact the surface energetics and carrier mobilities of monolayer MoS_2.[14,32–34] Experimental and theoretical results show that O_2 and/or H_2O molecules convert negative trions (a bound quasi-particle consisting of two electrons and one hole) in photoexcited as-prepared *n*-type MoS_2 into neutral excitons,[23,24] resulting in dramatically enhanced PL. Furthermore, Oh *et al.* demonstrated that laser irradiation on chemical-vapor-deposited (CVD) MoS_2 led to physisorbed O_2 on the surface, resulting in an initial increase in PL; further laser irradiation of MoS_2 under an O_2 environment photo-oxidized the MoS_2 *via* chemisorption and structurally damaged the monolayer MoS_2.[22] Sivaram *et al.* demonstrated a 200-fold PL enhancement from MoS_2 under

a. *Materials and Chemical Science and Technology Directorate, National Renewable Energy Laboratory, 15013 Denver West Parkway, Golden, Colorado 80401, United States.*
b. *Renewable and Sustainable Energy Institute, University of Colorado Boulder, Boulder, Colorado 80309, USA Address here.*
c. *Center for Integrated Nanostructure Physics (CINAP), Institute for Basic Science (IBS), Suwon, 16419 Republic of Korea*
d. *Department of Energy Science, Sungkyunkwan University, Suwon, 16419 Republic of Korea*
* Corresponding Authors: Elisa.Miller@nrel.gov

ambient conditions and proposed the surface reaction between MoS_2 and H_2O.[31] A recent report indicates O_2 may replace sulfur on MoS_2 at ambient conditions.[35] Similar PL enhancement was also observed within monolayer WS_2 *via* light irradiation under ambient conditions; however, the O_2 and H_2O vapor effects were not separated.[25,29,36] Lee *et al*. described the WS_2 PL enhancement as due to O_2 adsorbed at light-induced defects or reduction of exciton-exciton annihilation.[29] Another very recent report also found that illumination of WS_2 monolayers in ambient conditions (O_2 + H_2O) can potentially lead to photoinduced damage, although the exact mechanism of the damage is unclear and they were not able to separate O_2 and H_2O effects.[30] Moreover, this WS_2 report did not mention if this process was reversible or not. All of these observations highlight the susceptibility of monolayer TMDC properties to environmental conditions of the measurements and the importance of probing the optoelectronic properties for each TMDC in different environments.

It is still unclear whether O_2 *and/or* H_2O vapor will have identical effects when adsorbed onto WS_2 monolayers. To the best of our knowledge, controlled-environment optical experiments have not been conducted that decompose the impact of O_2 and H_2O vapor on the monolayer WS_2 optoelectronic properties. Without fully isolating these environmental conditions, it is difficult to distinguish chemical/physical phenomena. Here, we study the individual effects of O_2 and H_2O vapor by addressing these three questions: 1) What effects on optoelectronic properties are introduced by O_2 or H_2O vapor under illuminated conditions compared to the inert gas? 2) Are these effects reversible? And 3) if there are notably different effects from O_2 or H_2O, can WS_2 monolayers be used to detect relative humidity?

We employ CVD-grown monolayers of WS_2 for the O_2 and H_2O impact studies by subjecting the WS_2 monolayers to inert gas, dry air, and humid saturated nitrogen. With well-controlled environmental conditions, we examine monolayer WS_2 with PL and time-resolved microwave conductivity (TRMC) to monitor and probe the radiative recombination and charge carrier formation. The PL is decomposed as a function of laser power and exposure time to determine how the radiative pathways evolve, where the WS_2 PL consists of exciton (X^0), negative trion (X^-), and lower energy state(s) (LES – consist of localized defects and biexcitons) contributions.[37–39] The experimental results show O_2 and H_2O interact with WS_2 differently. These fundamental findings provide a better understanding of the impact of the local environment on optoelectronic properties, and in practice, allows us to utilize the monolayer WS_2 PL as an optical humidity sensor.

Experimental

Sample Preparation. Monolayer WS_2 is grown on SiO_2/Si wafers by atmospheric pressure CVD (APCVD), following the procedures from a previous report.[40] For synthesizing monolayer WS_2, a water-soluble precursor is coated on the

SiO_2/Si substrate first. The precursor solution is prepared by mixing three types of chemical solutions. 0.2 g of ammonium metatungstate (AMT, Sigma-Aldrich, 463922) apparent in 10 mL of deionized (DI) water for the tungsten precursor. 0.1 g of sodium hydroxide (NaOH, Sigma-Aldrich, 795429) dissolved in 30 mL DI water is introduced for promoting monolayer TMDC growth. An OptiPrep density gradient medium (Sigma-Aldrich, D1556, 60% (w/v) solution of iodixanol in water) is used as a medium solution. The mixed precursor solutions are coated onto the SiO_2/Si wafer by spin-casting at 3000 rpm for 1 min. The precursor-coated substrate and 0.2 g of sulfur (Sigma-Aldrich, 344621) are separately placed into a two-zone furnace. The temperature of the sulfur zone is increased to 220 °C at a rate of 25 °C/min while the substrate zone is increased to 800 °C at a rate of 100 °C/min. 600 sccm of N_2 and 10 sccm of H_2 gas are injected as a carrier gas and reactive agent, respectively, to reduce metal oxides. The as-grown WS_2 on SiO_2/Si is transferred to the quartz substrate for characterization. Poly(methyl methacrylate) (PMMA C4, MicroChem) is coated onto samples as a supporting layer and then immersed into diluted hydrofluoric acid for detaching WS_2 from the SiO_2/Si wafer by etching silicon oxide. The PMMA-supported samples are transferred to the quartz substrates and then PMMA was removed by acetone.

After growth via CVD, all the WS_2 monolayers are annealed at 300 °C in a glovebox with N_2 for 60 min to desorb any potential physisorbed molecules (as Step 1 in Schematic S1). We designed a sealed sample holder (diameter × height: 50 mm × 7 mm) containing two glass windows and one X-Profile Viton fluoroelastomer O-ring, which is robust enough to maintain the preferred environment for the duration of the measurements (at least 24 h). We encapsulate the WS_2 sample within the air-free holder in a N_2 glovebox (Step 2 in Schematic S1) and proceed to the optical measurements (Step 3 in Schematic S1). The humid saturated nitrogen condition is created by a humidifier contained purged 18.2 MΩ water in the N_2 glove bag (Step 2' in Schematic S1) with a humidity meter. To generate an O_2 rich environment, we use in-house dry air (~22 vol.% O_2 in N_2) to purge a glove bag for 3 h (Step 2'' in Schematic S1). Inert gas (N_2 only, 0% relative humidity), dry air (O_2 in N_2, 0% relative humidity), and humid N_2 (H_2O vapor in N_2) environments are at atmospheric pressure (~640 Torr). For the relative humidity experiments, we place the humidifier in the N_2 glove bag and added dry air, where the relative humidity is measured with a humidity meter.

Confocal Photoluminescence and Raman. Confocal PL and Raman spectra of WS_2 monolayers are acquired with an InVia Renishaw confocal Raman microscope with a 532-nm laser. We use a long working distance 50× objective lens (Olympus SLMPLN 50X Objective) with a numerical aperture of 0.35. The estimated laser-focused spot area is about 2.7 µm². A Thorlabs PM100D Power Meter measures the laser power. For the PL measurements, the laser intensities are between 6.5 µW and 12.9 mW with 2 s integration time and 5 accumulations. For the Raman measurements, the laser intensity is 1.84 kW/cm². The

sample reflected signal is dispersed (600 lines/mm grating for the PL measurements and 1800 lines/mm grating for the Raman measurements) and detected by a charge-coupled device (CCD) array. The *in-situ* PL scan is collected every 2 s with continuous laser exposure. The samples are fixed on a motorized stage. We collect the PL mapping data with 1-μm step sizes.

Time-resolved Microwave Conductivity. TRMC is used to measure the photoconductivity of the monolayer WS_2 reported herein. The measurement apparatus and details of the data analysis have been described extensively elsewhere.[41,42] Briefly, the measurement consists of monitoring the absorption of a 9 GHz continuous-wave microwave probe following photoexcitation of the sample with a few-nanosecond laser pulse. The measured microwave absorption is used to calculate the real part of the photoconductivity, which can, in turn, be expressed as the product of photoinduced charge carrier yield (ϕ) and the sum of the electron and hole mobilities ($\Sigma\mu$). The time resolution of the experiment, as configured here, is ~ 1 ns after the de-convolution of the instrument response function. All experiments reported herein are carried out in a sealed microwave cavity (K = 24000), actively purged with dry N_2.

Results and Discussion

We first monitor optoelectronic changes to the monolayer WS_2 under different environmental conditions with a combination of Raman, absorption, and PL measurements. In our sample film, the as-grown WS_2 monolayers (~20 μm in width, Figure 1a) are transferred onto quartz substrates (10 cm x 5 cm) and are then annealed in a N_2 glove box. Samples that are maintained in this environment are referred to as "N_2". Alternatively, we expose the thermally annealed samples to dry air (~22 vol.% O_2 in N_2) for one hour and label as "O_2" or expose the samples to H_2O vapor in N_2 for one hour and label as "H_2O". Throughout this study, we reuse one quartz substrate by annealing in an inert atmosphere (unless otherwise specified), which contains many WS_2 monolayers and few-layer triangles (Figure 1) and alternate the type of environment. Each measurement is repeated 2 – 5 times. When using confocal Raman and PL, we probe the same monolayer triangles for repeated measurements. The effects

seen in O_2 or H_2O environments are reversible upon re-annealing in N_2, which will be discussed in more detail in a subsequent section. For the absorption and TRMC measurements, we average over the entire substrate, which contains mostly monolayers (~75%) and some few-layers.

The Raman spectra for annealed, CVD-grown WS_2 has the expected in-plane mode E_{2g} and out-of-plane mode A_{1g} (Figure 1b), which supports high purity WS_2 monolayers.[43] The Raman spectra do not show apparent changes when WS_2 is exposed to the different environmental conditions (Figures S1), suggesting the overall structure of WS_2 remains unaffected. The WS_2 absorption spectra are shown in Figure 1c for the three controlled environments. The A and B excitons are observed at 610 and 510 nm, which agrees with reported values.[44,45] We do observe a lower energy shoulder on the A exciton, which is present under all environments. We believe that this is due to few-layers.[44,46,47]

Photoluminescence of CVD monolayer WS_2. PL is a particularly useful tool to determine the properties of WS_2 monolayers, such as film quality, thickness, doping levels, etc. Based on previous experimental reports and peak assignments, the WS_2 PL can be interpreted as arising from four different components: X^0, X^-, localized states, and biexcitons. The weighting or distribution of these contributions can lead to very different overall PL peak positions and shapes, which can be modulated by sample quality, excitation power density, as well as environmental factors, such as temperature, substrate, doping level, and ambient conditions.[48–50] Localized-states refer to defect-related emissions, which are often characterized as defect-bound excitons, and biexcitons refer to the Coulomb-bound complex of two excitons.[51–53] Specifically, emission from the lower energy, localized states appears below the exciton/trion and is often found in CVD WS_2 where the monolayers may contain numerous defects, which are believed to be sulfur vacancies. [49,54,53,55,56,38] Several studies also identify biexciton emission in CVD WS_2 monolayers, below the exciton/trion, by increasing the excitation power at cryogenic or room temperatures.[51,52] In our study, we do not separate defect and biexciton emission states and identify them collectively as
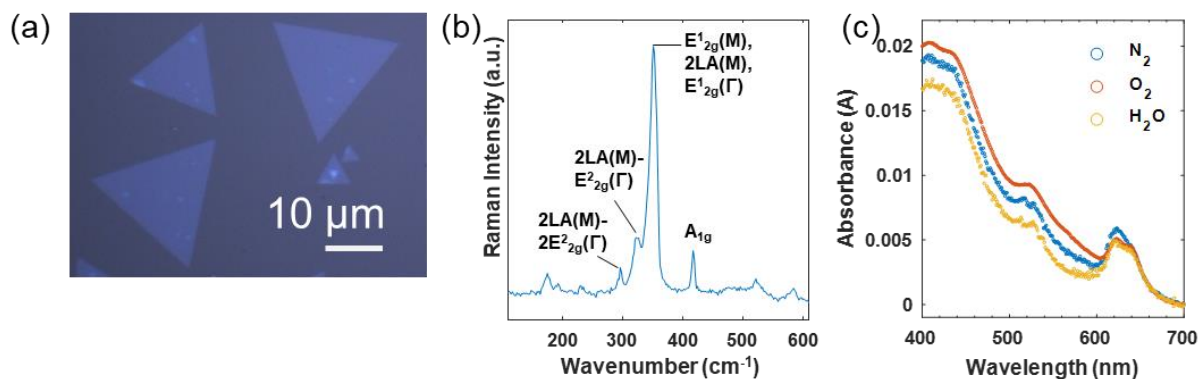

Figure 1. (a) Microscope image of CVD monolayer WS_2. (b) Raman spectrum of monolayer WS_2 exposed to N_2; the spectrum is representative of WS_2 exposed to the various environments, as no appreciable changes are observed for different environments (See Figure S1). (c) Absorption spectra of the WS_2 in three different environments.

LES in our decomposed PL. One would expect that at lower excitation power, the defect states would be the main contributor, while at higher excitation power, bi-exciton states would dominate the LES emission. Still, a single Gaussian curve may not completely capture all of the states comprising of the LES, especially at higher excitation power. However, the fitting and spectral complexity at higher excitation powers does not affect our data interpretation and conclusions at low to moderate excitation powers.
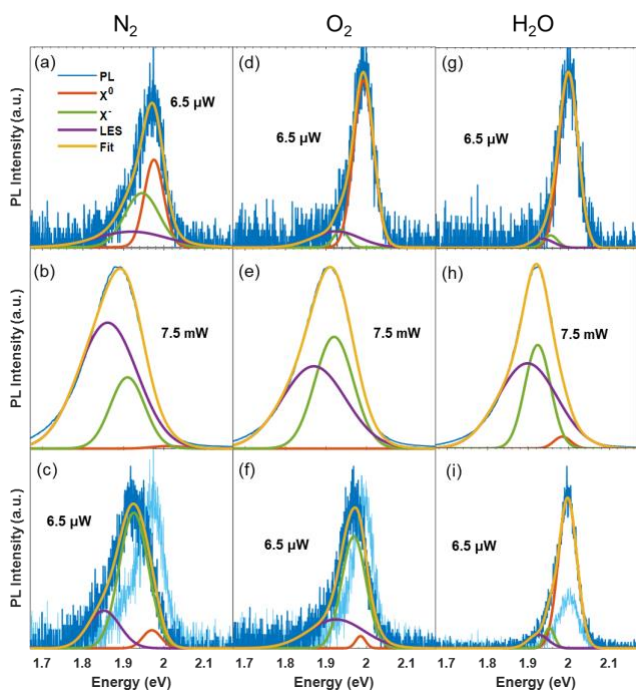

Figure 2. Monolayer WS_2 PL changes via laser power cycling of 532-nm laser irradiation under N_2 (a – c), O_2 (d – d), and H_2O (g – i) conditions. As the laser power is varied, the laser position on the WS_2 is the same; however, the laser spot is different for each environment. These measurements are repeated 5 times with similar results each time. The excitation power increases from 6.5 μW (a, d, g) to 7.5 mW (b, e, h) and extends to the highest power (12.9 mW, Figure S2), and then decreases back to 6.5 μW (c, f, i) for monolayer WS_2 in the N_2, O_2, and H_2O environment. Here, we demonstrate the second-highest excitation power (7.5 mW) data for clarity and consistency since the 12.9 mW can saturate the detector. For Figure a-i, dark blue lines are the collected PL results from the measurements. The red/green/purple represent X^0/X^-/LES Gaussian fits for the monolayer WS_2 PL spectra, respectively, and the yellow traces are the sum of the three Gaussian components to give the overall fit. For comparison, (c, f, i) also contain the original low energy PL from panel (a, d, g) as a light blue trace.

Excitation-Power Dependent PL Studies. We rely on the laser power-dependent PL to decompose the PL into three Gaussian components: X^0, X^-, and LES, as shown in Figure 2 and Figure S2. The PL is measured as the laser power is cycled twice, where one cycle is from low to high to low excitation power (6.5 μW to 12.9 mW to 6.5 kW with a laser focus area of 2.7 μm^2), without moving the laser spot. Additional Gaussian fitting details are provided in the caption of Figure S2. A sampling of power-dependent PL spectra for the monolayer WS_2 in N_2, O_2, and H_2O are demonstrated in Figure 2 for the first laser power cycle; the PL spectra for each environment for two complete power cycles are shown in Figure S2. For the first PL power-dependent cycle, the integrated intensities and percentage contribution for the

X^0, X^-, and LES peaks extracted from spectral decomposition are shown in Figure 3 and Figure S3, respectively. The FWHM of each component is in Figure S4. For the second power cycle, the integrated intensities and percentage contributions are shown in Figure S5.

The excitation power significantly impacts the WS_2 PL properties in a N_2 environment (Figures 2a-c and 3a). At low excitation power (6.5 μW), X^0 and X^- are about 37% and 40%, respectively, of the total PL (Figure 2a). As the laser power is increased, the overall PL peak position shifts to lower energy (~100 meV in Figure 2b), and the PL intensity increases. The decomposition of the spectrum taken at 7.5 mW demonstrates that the overall WS_2 PL change is dominated by a large increase in the LES contribution (Figure 2b). The PL at higher laser power (7.5 mW) is approximately 77% LES and 22% X^-, which are formed from a higher concentration of photoexcited X^0 and free carriers and results in a substantial increase of biexciton and trion emission.[39,52] Our results suggest that the overall redshift is due to a redistribution of the radiative pathways; however, at the higher powers, we cannot rule out the possibility that the shift is due to bandgap renormalization or laser-induced thermal effects.[50,57,58] Upon returning to the lowest excitation power, the original 6.5 μW WS_2 PL is not recovered, and the overall PL has redshifted due to a decrease in the X^0 contribution to 7% and an increase in the X^- contribution to 71%. In Figure 2c, we emphasize this difference by plotting the original PL spectrum from Figure 2a as light blue and the PL spectrum after one laser power-dependent cycle as dark blue. The second round of the laser power cycle does not induce further PL changes (Figures S2 and S5).

The power-dependent PL of monolayer WS_2 in an O_2 environment (Figures 2d-f and 3b) is different from the N_2 case. Initially, at low excitation power (Figure 2d), X^0 dominates the PL with 76% of the integrated intensity, which leads to a narrower overall PL shape than the N_2 case. At high excitation power (Figure 2e), the O_2 case is dominated by LES, where the X^-/LES emissions are 36% and 63%, respectively and is similar to the N_2 case. As the power is cycled back down, there is a slight PL redshift (Figure 2f) that is due to a decrease of the X^0 to 6%. The Gaussian fitting reveals that the X^- component is about ~60% of the overall intensity, which is a similar trend to the N_2 case. One interesting difference between the WS_2 PL changes in O_2 compared to N_2 is that that second power-dependent cycle leads to an increased PL intensity (Figures S2 and S5). This is due to the X^-/LES increasing in intensity, which gives an overall higher PL quantum yield on the 2nd excitation power cycle.

As for the H_2O case, the WS_2 PL properties are very different (Figures 2g-I and 3c) as a function of the laser power cycling. Initially, at low excitation power (Figure 2g), the overall PL intensity is low compared to the N_2 and O_2 case, and the PL is mainly composed of emission from X^0, which is about 92%, resulting in a narrower PL. At higher excitation power in Figure 2h, the PL spectrum is also narrower compared to the N_2 and O_2
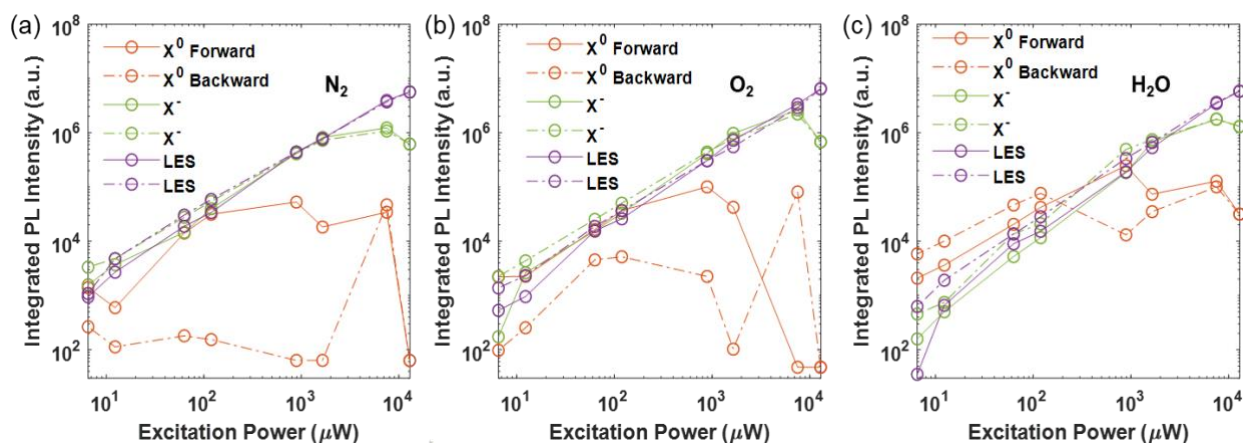
Figure 3. Integrated PL area of X^0, X^-, and LES as a function of excitation power derived from the Gaussian fitting results from Figure 2 and Figure S2 for the three environments, (a) in N_2, (b) O_2, and (c) H_2O. The solid and dash lines represent the PL change as the excitation power ascends and descends, respectively, for the first laser power cycle. Corresponding FWHM is shown in Figure S4. The integrated PL intensity for the 2nd laser power cycle is shown in Figure S5.

cases; this is due to blue-shifting of LES emission and a smaller FWHM of X^- emission. As the excitation power is cycled back down (Figure 2i), WS_2 demonstrates a significant PL increase and the same peak position as compared to the original PL at 6.5 µW. At low excitation power at the end of the first power cycle, X^0 emission is still the main contributor (84%) to the WS_2 PL in an H_2O environment, which is a very different phenomenon than WS_2 in N_2 or O_2 environments (Figure 2 c, f, i). The 2nd excitation power cycle does not result in any additional changes and parallels the first cycle (Figures S2 and S5).

The decomposed PL contributions are summarized in a log-log plot in Figure 3, where solid traces represent the increasing excitation power and dashed traces describe the decreasing excitation power for the first power cycle. It is worth noting that at higher excitation power, the X^0 contribution is minor; therefore, the Gaussian fitting results of the X^0 may be less accurate compared to the X^-/LES fits. For all three cases as the laser power increases, the overall PL intensity increases, which is expected. However, the spectral weightings change as the laser power is increased. Specifically, the relative WS_2 X^0 contribution decreases while X^- and LES increase. As the power is cycled back down, the three cases vary. The WS_2 in N_2 and O_2 environments do not recover the original component contributions of the PL at low power and have little to no X^0 contribution (36% to 6% for N_2 and 76% to 6% for O_2), whereas component contributions of the WS_2 PL in H_2O retain a similar level, i.e., the X^0 is still the main contributor (92% to 84%). The spectral contributions as a function of ascending laser power have been fit to a line and are shown in Figure S6 and Table S1. The power cycle measurements of Raman spectra in all three environments do not have any apparent changes; the details are provided in Figure S7.

Excitation-Time Dependent PL Studies. To further investigate photochemical insight into the effects of illumination and environment on WS_2 PL, we carry out *in-situ* monitoring of the PL upon continuous 532-nm laser illumination. Here, we

decompose the overall WS_2 PL into the X^0, X^-, and LES contributions as a function of exposure time with 119-µW, 532-nm illumination for 1000 s. The PL spectra before and after laser exposure along with the decomposed relative intensities versus laser irradiation time are shown in Figure 4 for each environment. For the N_2 case, Figure 4a depicts the PL spectra of the WS_2 before and after the 1000-s laser irradiation. The overall PL peak center shifts from 1.99 eV to 1.96 eV, rendering a ~30 meV redshift. This redshift is comparable to the ~40 meV shift that we observe in the low-power PL measurements before and the first laser power cycle (Figure 2c), suggesting long-time, moderate power laser irradiation triggers a very similar process as the short-time irradiation with high-power. The overall PL change is due to a decrease in the X^0 contribution in combination with an increase in both X^- and LES contributions until reaching a steady magnitude after ~600 seconds (Figure 4b). We verify that the Raman spectra do not change under these conditions, suggesting the monolayer WS_2 crystal structure may not change significantly (Figure S8-S10). We note
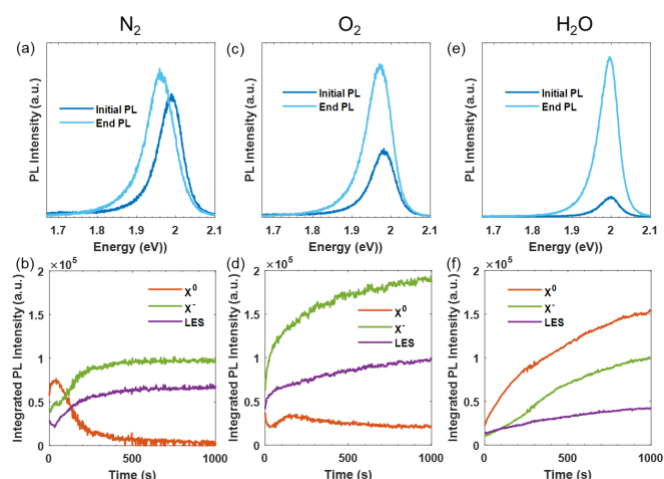

Figure 4. (a, c, e) PL intensity of monolayer WS_2 before (blue) and after (light blue) 1000 s of continuous 532-nm laser illumination in N_2, O_2, and H_2O, respectively. (b, d, f) The individual fits are shown in Figure S11. For each environment, the overall PL is decomposed into three Gaussians, corresponding to X^0 (red), X^- (green), and LES (purple) emission intensities vs. illumination time. The laser intensity is 119 µW.
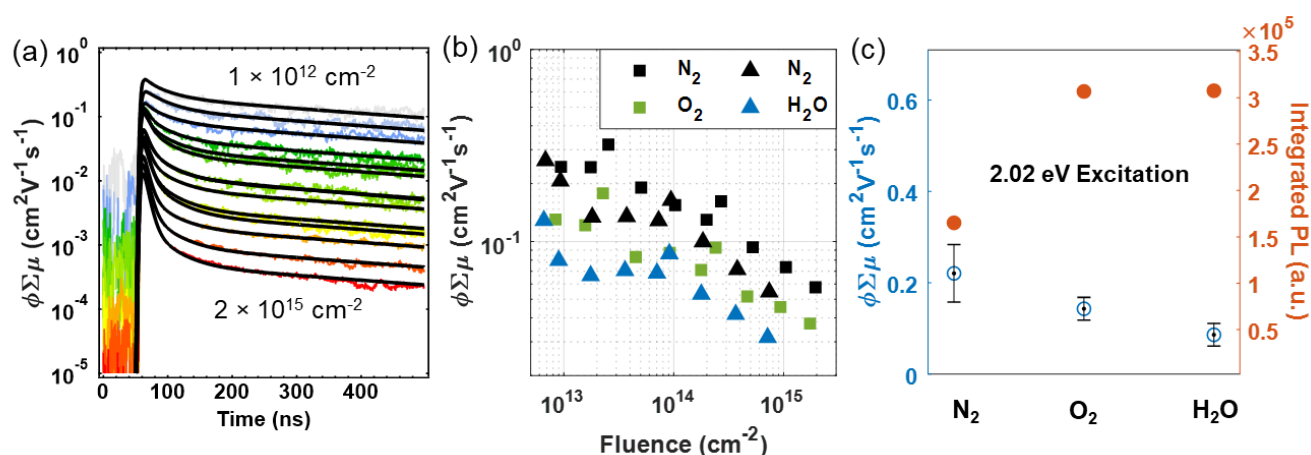
Figure 5. (a) Representative photoconductivity transients at 2.02 eV (X^0) excitation as a function of absorbed laser fluence for annealed WS_2, expressed as the yield-mobility product. The black lines are from a global fit to a sum of three exponentials (τ_1 = 2.6 ns, τ_2 = 34 ns, and τ_3 = 580 ns). (b) Yield-mobility products vs. excitation fluence and (c) extracted average yield-mobility products (blue) of the WS_2 in N_2, O_2, and H_2O at an incident laser fluence of 1.3 – 2 ×10^{13} cm^{-2} along with the PL integrated area at t = 1000 s (red) from Figure 4.

that Raman spectroscopy is not sensitive to single point defects and will only be affected at high defect concentrations.[59,60]

When we analyze the WS_2 PL under an O_2 environment, at t = 0 s, there are not any apparent spectral differences from the N_2 case. During the 1000 s of 532-nm illumination (Figure 4c), we observe significant differences compared to the N_2 environment. The WS_2 PL intensity after laser irradiation increases by more than a factor of 2 along with a ~10 meV redshift of the peak position, which is consistent with the results at low power following two power-dependent cycles (Figure S2 and Figure S5). This PL enhancement is reversible via thermal annealing in an inert gas (Figure S12) and was shown on a second set of MoS_2 monolayers (details see Figure S14). The reversibility, which applies to all three environments, allows us to repeat measurements on the same WS_2 monolayers. Figure 4d demonstrates that the overall PL change is mostly due to the increased X^- contribution, which more than doubles in area with time, as well as the LES contribution, which grows in area by ~1.5. The growth of the X^- and LES contributions increases the overall WS_2 PL intensity and redshifts the PL peak position. The X^0 changes little with laser illumination but does have some fluctuation during the first 300 s.

The WS_2 PL in an H_2O environment shows a distinct behavior following laser illumination compared to the N_2 and O_2 environments (Figure 4e and 4f), which is similar to the laser power-dependent measurements. At t = 0 s, the overall WS_2 PL intensity is minimized, narrower, and blue-shifted compared to the N_2 case. However, following 1000 s of laser illumination in H_2O, the WS_2 PL increases by a factor of ~7, while the overall PL shape and peak position remains nearly identical. The quantum yield enhancement is due to increased emission from all three radiative pathways, where X^0 is the main contributor, contributing about 50% of the total emission before and after illumination. The explanation to the different PL behaviors will be discussed in the *Proposed Mechanism Section*.

Photoconductivity. We use TRMC to evaluate the influence that environmental molecules (N_2, O_2, and H_2O) have on long-lived (τ > 1 ns) photoconductivity when exciting at the X^0 transition (2.02 eV) transition, which should selectively excite WS_2 monolayers. Several previous photoconductivity studies of TMDCs utilized time-resolved terahertz spectroscopy (TRTS) to assess the ultrafast dynamics related to initial carrier trapping, thermalization, and exciton formation (100 fs – 1 ns).[61–67] Using microwave conductivity enables the use of laser fluences 2 orders of magnitude lower than are typically utilized for TRTS studies, providing data in a fluence regime that (1) is less affected by non-linear (*e.g.*, Auger) processes that can reduce charge carrier yield and lifetime, and (2) may be more relevant to photoelectrochemical applications of these materials that would proceed at low fluence.

The TRMC results are shown in Figure 5. Panel (5a) gives the photoconductivity transients for annealed WS_2, expressed as the product of charge carrier yield and the sum of the electron and hole mobilities ($\phi\Sigma\mu$). These transients are representative of all sample conditions investigated, in that the shape and trend with fluence are not dramatically altered by exposure to O_2 or H_2O vapor. The black fit lines result from a global fit to the fluence-dependent data using the sum of three exponentials with time constants of τ_1 = 2.6 ns, τ_2 = 34 ns, and τ_3 = 580 ns; we carry out this fitting procedure for all of our WS_2 TRMC measurements in order to parameterize the data and make sensible comparisons between sample conditions. WS_2 photoconductivity and dynamics are strongly fluence-dependent (Figure 5a). At an incident absorbed photon fluence of 10^{15} cm^{-2}, the photoconductivity transient is dominated by a fast 2.6 ns component, which is near the resolution limit of our experiment as presently configured. At 10^{12} cm^{-2} the dominant decay component is 580 ns. These observations are consistent with bimolecular recombination being the dominant charge carrier loss process. This situation applies to all of the sample conditions we measure, but the signal magnitude and lifetime vary according to the WS_2 environment. The yield-mobility

products for the different laser fluences are depicted in Figure 5b. Figure 5c summarizes the results from Figure 5b analysis for WS_2 exposed to N_2, O_2, and H_2O conditions, comparing the average of the exponential amplitudes at an incident laser fluence (photons/pulse/area) between 1.3 and 2.0×10^{13} cm^{-2}. In addition, we include the PL integrated area at 1000 s extracted from Figure 4b, 4d, and 4f for comparison. The yield-mobility product and amplitude-weighted average lifetime versus absorbed fluences are summarized in Figure S15.

We make two clear observations from this TRMC data (Figure 5 and S15). First, exposing the sample to O_2 or H_2O vapor along with continuous 532-nm LED illumination for 12 h reduces the yield-mobility product and amplitude-weighted average lifetime compared to the annealed sample. Second, the yield-mobility product is anticorrelated with the PL integrated area. Interpreting microwave data is often complicated by the convolution of charge carrier yield and mobility. Following the initial generation of charges by the laser pulse (end-of-pulse $\phi\Sigma\mu$), the ensuing $\phi\Sigma\mu$ dynamics can be straightforwardly associated with the time-dependent density of mobile charges in the film because the relevant timescale (t >>100 ps) is much longer than that of carrier cooling. Thus, the main question is whether the different end-of-pulse $\phi\Sigma\mu$ values observed for WS_2 subjected to O_2 and H_2O exposure result from differences in the nanosecond yield or mobility of charge carriers.

In this context, the anticorrelation between the WS_2 PL and yield-mobility product data is instructive. In excitonic semiconductors, the PL quantum yield is directly proportional to the number of photogenerated excitons that survive non-radiative processes to recombine radiatively. In contrast, the TRMC yield-mobility product is insensitive to Coulomb-bound excitons, but instead requires processes (*e.g.*, spontaneous exciton dissociation, trapping, charge transfer, etc.) that transform the expected population of excitons into free electrons and/or holes. The concomitant enhancement of PL and reduction of $\phi\Sigma\mu$ is thus consistent with a photoinitiated reaction with O_2 or H_2O vapor, which passivates or compensates WS_2 surface defects that would otherwise capture one of the mobile charges prior to exciton formation (within 1 ps).[68] Equivalently the native WS_2 surface defects (before reaction with O_2 or H_2O molecules) could act to dissociate excitons on a tens of picosecond timescale.

Proposed Mechanism. By summarizing our PL and TRMC experimental observations, we propose a mechanism to interpret the role of the environment on the measured WS_2 optoelectronic properties. In the N_2 environment, the WS_2 PL distribution changes during the first laser-power dependent cycle and the initial 600 s of 532-nm, 119 μW laser exposure; therefore, we propose that the 532-nm illumination immediately desorbs residually adsorbed molecules on the WS_2 surface by a photo-induced desorption process, which is consistent with previously proposed mechanisms on TMDC surfaces with laser exposure.[55] Once this desorption occurs, there are no other photoreactions that occur on the WS_2

surface when in the N_2 environment, and the WS_2 PL remains constant during the second power cycle and the last 400 s of laser exposure. Another mechanism could be photodamage of the WS_2 surface.[29] However, photodamage is unlikely under our laser conditions since the PL change does not progress further, and, the PL changes are reversible (Figure S12 and S14). When annealed WS_2 is exposed to the N_2 environment and laser irradiation, the overall PL quantum yield change is minimal, while the photoconductivity is relatively high. As shown in Figure 6, it is possible that the light-induced degassing process drives adsorbents off the surface, exposing the defects and surface while changing the dominant excited-state emissive population from X^0 to X^-/LES. Based off of previous CVD grown reports, it is likely that these defects are sulfur vacancies.[37,38] Also, the character of the adsorbed surface molecules (labeled "R" in Figure 6) is still ambiguous, although we suggest that it is unlikely to be carbon-based doping, which would result in a sub-gap emission peak from WS_2, which was shown to be located 150 meV below the optical bandgap.[69] We hypothesis that these "R" molecules are likely physisorbed to the WS_2 surface following the anneal step while the sample is cooling in the glovebox. As an additional control, we also investigate the WS_2 PL change with 532-nm illumination in an Ar environment and measure very similar results, which strengthens our argument that the PL change is due to laser-induced desorption and not N_2 surface reactivity.
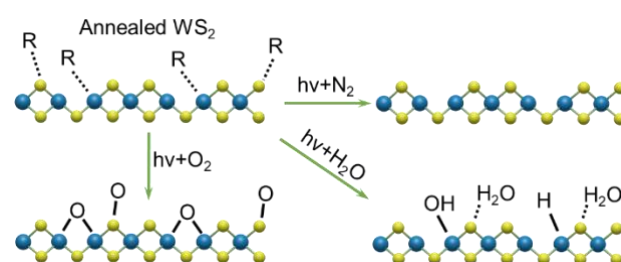

Figure 6. Proposed mechanism for WS_2 monolayer films exposed to N_2, O_2, and H_2O environments after (lower) 532-nm laser illumination. The real mechanism is not limited to the depicted surface reactions shown here.

The WS_2 PL with O_2 and 532-nm illumination is different from the N_2 case in that WS_2 PL intensity increases. Without illumination, O_2 molecules do not appear to interact strongly with the WS_2 basal plane, but it is possible that O_2 molecules may be physiosorbed at certain defects of WS_2.[25] With illumination, at early times, we propose that the laser exposure displaces the adsorbed gases; however, there is a subsequent photoreaction with the exposed WS_2 surface/defects and O_2. Therefore, we propose that the photoreaction on the surface is responsible for the loss of photoconductivity and the increase in PL yield when WS_2 is exposed to an O_2 environment and 532-nm illumination. Based on the power-dependent cycling (Figure 3b), we hypothesize that the first laser power cycle desorbs the adsorbed chemicals from sulfur vacancies, like the N_2 case, reduces the X^0 contribution and increases the X^- contribution, and opens the vacancy sites for further reactions. The second laser power cycle induces the photo-oxidation between WS_2

and O_2, where oxygen may substitute the sulfur vacancies, leading to an overall quantum yield increase. Such a process has been reported for other TMDCs, such as $MoSe_2$.[46] In the in-situ laser irradiation measurement (Figure 4d), the overall PL continuously increases, while residual molecules are being desorbed and photooxidation is occurring.

The H_2O molecules strongly influence WS_2 in the dark. It is likely that the low, blue-shifted narrow PL emission in the dark is due to physisorbed H_2O molecules across the monolayer surface,

Relative Humidity Sensing. WS_2 interacting with O_2 or H_2O under continuous laser exposure have distinct radiative pathways. Thus, we expect that the PL will vary under different relative humidity conditions when exposed to 1000 s of continuous 532-nm laser illumination, where the relative humidity is the amount of H_2O in dry air. Here, we investigate 40% and 80% relative humidity to test our hypothesis (Figure 7). At 40% relative humidity (Figure 7a), the WS_2 PL change after 1000 s of continuous 532-nm laser illumination is characteristic
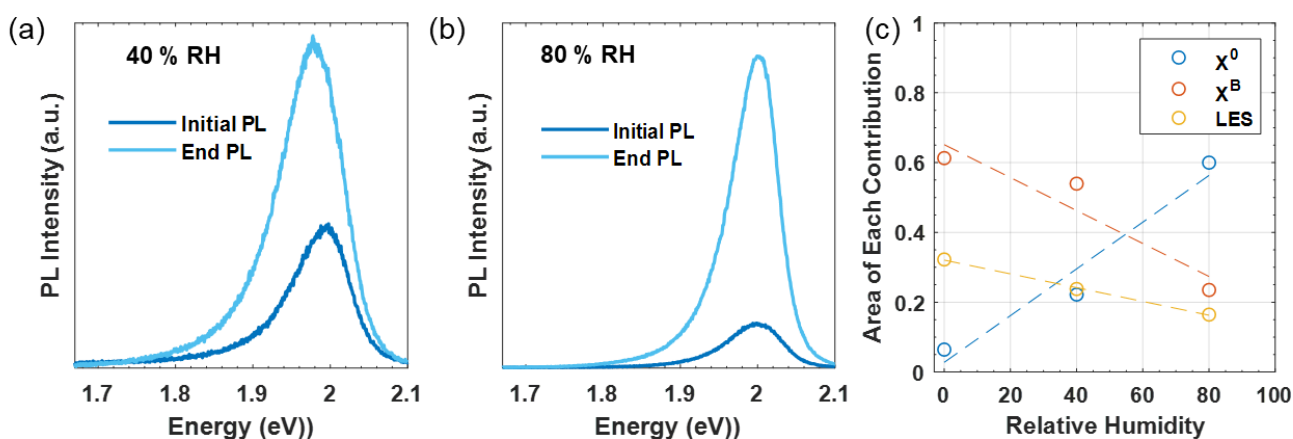

Figure 7. PL spectra before (dark blue) and after (light blue) 1000-s laser irradiation of the WS_2 monolayer, for (a) 40% and (b) 80% RH, respectively. The decomposed PL is shown in Figure S16. (c) The decomposed PL Gaussian fitting area contribution for the X^0, X^-, and LES contributions as a function of relative humidity. The lines in Figure 7c are linear fittings for each component. Note RH = relative humidity, which is the amount of H_2O in dry air.

which may change the dielectric constant of the WS_2 surface (Figure 2g at low laser power and Figure 4e and 4f at t = 0 s).[70] With continuous 532-nm illumination, H_2O molecules likely photoreact with WS_2 surface and defects, while displacing the original physisorbed molecules at defects that are labeled "R" and physisorbed H_2O molecules in Figure 6. Interestingly, Peimyoo et al. demonstrated that the PL of WS_2 submerged in water and exposed to laser excitation reveals PL emission that is dominated by X^0, an effect attributed to p-type doping by water.[3] They observe a similar phenomenon of X^0 appearance as a function of H_2O and light exposure without ruling out an O_2 effect. Here, due to the initial PL from all three cases having strong X^0 contribution but only the H_2O case possessing the X^0 PL contribution after laser illumination, we argue the initial adsorbing chemicals have similar effects (photo-doping or photo-induced hydrogenation reaction) as H_2O on WS_2. The initial X^0 from the WS_2 in all three cases is possible from a p-type doped WS_2 monolayer by "R". For the H_2O environment, H_2O molecules may play a role as p-type dopants by adding hydroxyls, or hydrogenating defects, onto sulfur vacancies and/or the basal plane of the WS_2 after light illumination, enhancing the X^0 emission.[29,71] It is worth noting that our proposed mechanism is different than the hypothesized mechanism by Sivaram et al., where they suggest the H_2O may react with the MoS_2 surface by filling the surface vacancy with oxygen and generating hydrogen molecules.[31] Since our observation between O_2 and H_2O are quite different in terms of peak shifting and intensity enhancement, the possible reaction products should be different.

of WS_2 exposed to the O_2 environment, where there is an overall PL redshift in addition to a PL increase. The decomposed PL as a function of time shows that the X^- emission is dominating the PL increase (Figure S16a). In the 80% relative humidity environment shown in Figure 7b, the WS_2 PL increases in intensity with minimal shifting, which follows the trend of the H_2O environment only. The X^0 emission (~52% at t = 1000 s from ~60% at t = 0 s) governs the overall quantum yield increase, as seen from Figure S16b. In summary, WS_2 PL changes in the 40% and 80% relative humidity environment are very distinguishable and agree with our O_2 and H_2O only environments, providing a unique way to quantify the relative humidity. A summarized X^0, X^-, LES distribution against relativity humidity (including the 0% relative humidity PL data in Figure 4) are plotted in Figure 7c. The linear relationship between each component versus relative humidity supports our proposed mechanism.

Conclusions

We disentangle the O_2 and H_2O vapor effects on the optoelectronic properties of monolayer WS_2 by exposing WS_2 to well-controlled environments. PL measurements demonstrate that O_2 and H_2O vapor with 1000 s of continuous 532-nm illumination induces higher WS_2 PL emission by a factor of 2 and 7, respectively. The PL decomposition after laser exposure indicates that the WS_2 X^- emission dominates when WS_2 is in the O_2 environment, whereas X^0 dominates the WS_2 PL in an H_2O environment. We propose that upon 532-nm illumination, both O_2 and H_2O molecules undergo reversible surface reactions,

thereby enhancing PL. Using TRMC, we determine that both O_2 and H_2O vapor decrease the WS_2 photoconductivity, which is anticorrelated with the increased PL. Our ability to disentangle the O_2 and H_2O effects on WS_2 optoelectronic properties enables us to detect relative humidity with WS_2 PL and continuous 532-nm illumination. Our results directly contribute to the ongoing research regarding the potential applications of WS_2 in the area of photocatalysis, optoelectronics, and gas sensors.

Conflicts of interest

The authors declare no competing financial interests.

Acknowledgments

References

1   M. W. Iqbal, M. Z. Iqbal, M. F. Khan, M. A. Shehzad, Y. Seo and J. Eom, *Nanoscale*, 2015, **7**, 747–757.
2   H. Song, X. Yu, M. Chen, M. Qiao, T. Wang, J. Zhang, Y. Liu, P. Liu and X. Wang, *Applied Surface Science*, 2018, **439**, 240–245.
3   N. Peimyoo, W. Yang, J. Shang, X. Shen, Y. Wang and T. Yu, *ACS Nano*, 2014, **8**, 11320–11329.
4   J. Choi, H. Zhang and J. H. Choi, *ACS Nano*, 2016, **10**, 1671–1680.
5   P. Choudhury, L. Ravavarapu, R. Dekle and S. Chowdhury, *J. Phys. Chem. C*, 2017, **121**, 2959–2967.
6   P. Huang, Z. Wang, Y. Liu, K. Zhang, L. Yuan, Y. Zhou, B. Song and Y. Li, *ACS Appl. Mater. Interfaces*, 2017, **9**, 25323–25331.
7   Y. G. Kim, K. C. Kwon, Q. V. Le, K. Hong, H. W. Jang and S. Y. Kim, *Journal of Power Sources*, 2016, **319**, 1–8.
8   K. Kang, S. Xie, L. Huang, Y. Han, P. Y. Huang, K. F. Mak, C.-J. Kim, D. Muller and J. Park, *Nature*, 2015, **520**, 656–660.
9   K. Y. Ko, J.-G. Song, Y. Kim, T. Choi, S. Shin, C. W. Lee, K. Lee, J. Koo, H. Lee, J. Kim, T. Lee, J. Park and H. Kim, *ACS Nano*, 2016, **10**, 9287–9296.
10 K. Chang, M. Li, T. Wang, S. Ouyang, P. Li, L. Liu and J. Ye, *Advanced Energy Materials*, 2015, **5**, 1402279.
11 H. Zhang, J. Choi, A. Ramani, D. Voiry, S. N. Natoli, M. Chhowalla, D. R. McMillin and J. H. Choi, *ChemPhysChem*, 2016, **17**, 2854–2862.

12 E. E. Benson, H. Zhang, S. A. Schuman, S. U. Nanayakkara, N. D. Bronstein, S. Ferrere, J. L. Blackburn and E. M. Miller, *J. Am. Chem. Soc.*, 2017, **140**, 441–450.
13 I. Paradisanos, N. Pliatsikas, P. Patsalas, C. Fotakis, E. Kymakis, G. Kioseoglou and E. Stratakis, *Nanoscale*, 2016, **8**, 16197–16203.
14 C. Zheng, Z.-Q. Xu, Q. Zhang, M. T. Edmonds, K. Watanabe, T. Taniguchi, Q. Bao and M. S. Fuhrer, *Nano Lett.*, 2015, **15**, 3096–3102.
15 J. Choi, H. Zhang, H. Du and J. H. Choi, *ACS Appl. Mater. Interfaces*, 2016, **8**, 8864–8869.
16 C.-J. Shih, Q. H. Wang, S. Lin, K.-C. Park, Z. Jin, M. S. Strano and D. Blankschtein, *Phys. Rev. Lett.*, 2012, **109**, 176101.
17 Y. Hu, Z.-H. Qi, J. Lu, R. Chen, M. Zou, T. Chen, W. Zhang, Y. Wang, X. Xue, J. Ma and Z. Jin, *Chem. Mater.*, 2019, **31**, 4524–4535.
18 T. Pham, G. Li, E. Bekyarova, M. E. Itkis and A. Mulchandani, *ACS Nano*, 2019, **13**, 3196–3205.
19 Z. Qin, D. Zeng, J. Zhang, C. Wu, Y. Wen, B. Shan and C. Xie, *Applied Surface Science*, 2017, **414**, 244–250.
20 Y. Luo, Y. Chen, K. Xia, S. Peng, H. Guan, J. Tang, H. Lu, J. Yu, J. Zhang, Y. Xiao and Z. Chen, *Opt. Express, OE*, 2016, **24**, 8956–8966.
21 J. Feng, L. Peng, C. Wu, X. Sun, S. Hu, C. Lin, J. Dai, J. Yang and Y. Xie, *Advanced Materials*, 2012, **24**, 1969–1974.
22 H. M. Oh, G. H. Han, H. Kim, J. J. Bae, M. S. Jeong and Y. H. Lee, *ACS Nano*, 2016, **10**, 5230–5236.
23 S. Tongay, J. Zhou, C. Ataca, J. Liu, J. S. Kang, T. S. Matthews, L. You, J. Li, J. C. Grossman and J. Wu, *Nano Letters*, 2013, **13**, 2831–2836.
24 H. Nan, Z. Wang, W. Wang, Z. Liang, Y. Lu, Q. Chen, D. He, P. Tan, F. Miao, X. Wang, J. Wang and Z. Ni, *ACS Nano*, 2014, **8**, 5738–5745.
25 A. Venkatakrishnan, H. Chua, P. Tan, Z. Hu, H. Liu, Y. Liu, A. Carvalho, J. Lu and C. H. Sow, *ACS Nano*, 2017, **11**, 713–720.
26 X. H. Wang, J. Q. Ning, Z. C. Su, C. C. Zheng, B. R. Zhu, L. Xie, H. S. Wu and S. J. Xu, *RSC Adv.*, 2016, **6**, 27677–27681.
27 A. Bera, D. V. S. Muthu and A. K. Sood, *Journal of Raman Spectroscopy*, 2018, **49**, 100–105.
28 H. R. Gutiérrez, N. Perea-López, A. L. Elías, A. Berkdemir, B. Wang, R. Lv, F. López-Urías, V. H. Crespi, H. Terrones and M. Terrones, *Nano Letters*, 2013, **13**, 3447–3454.
29 Y. Lee, G. Ghimire, S. Roy, Y. Kim, C. Seo, A. K. Sood, J. I. Jang and J. Kim, *ACS Photonics*, 2018, **5**, 2904–2911.
30 J. C. Kotsakidis, Q. Zhang, A. L. Vazquez de Parga, M. Currie, K. Helmerson, D. K. Gaskill and M. S. Fuhrer, *Nano Lett.*, 2019, **19**, 5205–5215.
31 S. V. Sivaram, A. T. Hanbicki, M. R. Rosenberger, G. G. Jernigan, H.-J. Chuang, K. M. McCreary and B. T. Jonker, *ACS Appl. Mater. Interfaces*, 2019, **11**, 16147–16155.
32 S. Y. Lee, U. J. Kim, J. Chung, H. Nam, H. Y. Jeong, G. H. Han, H. Kim, H. M. Oh, H. Lee, H. Kim, Y.-G. Roh, J. Kim, S. W. Hwang, Y. Park and Y. H. Lee, *ACS Nano*, 2016, **10**, 6100–6107.
33 J.-H. Ahn, W. M. Parkin, C. H. Naylor, A. T. C. Johnson and M. Drndić, *Scientific Reports*, 2017, **7**, 4075.
34 W. Park, J. Park, J. Jang, H. Lee, H. Jeong, K. Cho, S. Hong and Takhee Lee, *Nanotechnology*, 2013, **24**, 095202.
35 J. Pető, T. Ollár, P. Vancsó, Z. I. Popov, G. Z. Magda, G. Dobrik, C. Hwang, P. B. Sorokin and L. Tapasztó, *Nature Chemistry*, 2018, **10**, 1246.
36 P. Atkin, D. W. M. Lau, Q. Zhang, C. Zheng, K. J. Berean, M. R. Field, J. Z. Ou, I. S. Cole, T. Daeneke and K. Kalantar-Zadeh, *2D Mater.*, 2018, **5**, 015013.
37 P. K. Chow, R. B. Jacobs-Gedrim, J. Gao, T.-M. Lu, B. Yu, H. Terrones and N. Koratkar, *ACS Nano*, 2015, **9**, 1520–1527.
38 V. Carozo, Y. Wang, K. Fujisawa, B. R. Carvalho, A. McCreary, S. Feng, Z. Lin, C. Zhou, N. Perea-López, A. L. Elías, B. Kabius, V. H. Crespi and M. Terrones, *Science Advances*, 2017, **3**, e1602813.
39 Y. Lee, S. J. Yun, Y. Kim, M. S. Kim, G. H. Han, A. K. Sood and J. Kim, *Nanoscale*, 2017, **9**, 2272–2278.
40 S. J. Yun, G. H. Han, H. Kim, D. L. Duong, B. G. Shin, J. Zhao, Q. A. Vu, J. Lee, S. M. Lee and Y. H. Lee, *Nature Communications*, 2017, **8**, 2163.
41 O. G. Reid, D. T. Moore, Z. Li, D. Zhao, Y. Yan, K. Zhu and G. Rumbles, *J. Phys. D: Appl. Phys.*, 2017, **50**, 493002.
42 T. J. Savenije, A. J. Ferguson, N. Kopidakis and G. Rumbles, *J. Phys. Chem. C*, 2013, **117**, 24085–24103.

43 K. M. McCreary, A. T. Hanbicki, S. Singh, R. K. Kawakami, G. G. Jernigan, M. Ishigami, A. Ng, T. H. Brintlinger, R. M. Stroud and B. T. Jonker, *Scientific Reports*, 2016, **6**, 35154.

44 B. Zhu, X. Chen and X. Cui, *Scientific Reports*, 2015, **5**, 9218.

45 W. Zhao, Z. Ghorannevis, L. Chu, M. Toh, C. Kloc, P.-H. Tan and G. Eda, *ACS Nano*, 2013, **7**, 791–797.

46 L. Wang, M. Schmid, Z. N. Nilsson, M. Tahir, H. Chen and J. B. Sambur, *ACS Appl. Mater. Interfaces*, 2019, 11.

47 J. L. Blackburn, H. Zhang, A. R. Myers, J. R. Dunklin, D. C. Coffey, R. N. Hirsch, D. Vigil-Fowler, S. J. Yun, B. W. Cho, Y. H. Lee, E. M. Miller, G. Rumbles and O. G. Reid, *J. Phys. Chem. Lett.*, 2020, **11**, 99–107.

48 X. Fan, W. Zheng, H. Liu, X. Zhuang, P. Fan, Y. Gong, H. Li, X. Wu, Y. Jiang, X. Zhu, Q. Zhang, H. Zhou, W. Hu, X. Wang, X. Duan and A. Pan, *Nanoscale*, 2017, **9**, 7235–7241.

49 J. Li, W. Su, F. Chen, L. Fu, S. Ding, K. Song, X. Huang and L. Zhang, *J. Phys. Chem. C*, 2019, 8.

50 K. Wei, Y. Liu, H. Yang, X. Cheng and T. Jiang, *Appl. Opt., AO*, 2016, **55**, 6251–6255.

51 G. Plechinger, P. Nagler, J. Kraus, N. Paradiso, C. Strunk, C. Schüller and T. Korn, *physica status solidi (RRL) – Rapid Research Letters*, 2015, **9**, 457–461.

52 I. Paradisanos, S. Germanis, N. T. Pelekanos, C. Fotakis, E. Kymakis, G. Kioseoglou and E. Stratakis, *Appl. Phys. Lett.*, 2017, **110**, 193102.

53 T. Kato and T. Kaneko, *ACS Nano*, 2014, **8**, 12777–12785.

54 J. Shang, X. Shen, C. Cong, N. Peimyoo, B. Cao, M. Eginligil and T. Yu, 2015, **9**, 9.

55 Z. He, X. Wang, W. Xu, Y. Zhou, Y. Sheng, Y. Rong, J. M. Smith and J. H. Warner, *ACS Nano*, 2016, **10**, 5847–5855.

56 Z. He, W. Xu, Y. Zhou, X. Wang, Y. Sheng, Y. Rong, S. Guo, J. Zhang, J. M. Smith and J. H. Warner, *ACS Nano*, 2016, **10**, 2176–2183.

57 A. Chernikov, C. Ruppert, H. M. Hill, A. F. Rigosi and T. F. Heinz, *Nature Photonics*, 2015, **9**, 466–470.

58 H. Wang, J. Wen, W. Wang, N. Xu, P. Liu, J. Yan, H. Chen and S. Deng, *ACS Nano*, 2019, **13**, 1739–1750.

59 W. M. Parkin, A. Balan, L. Liang, P. M. Das, M. Lamparski, C. H. Naylor, J. A. Rodríguez-Manzo, A. T. C. Johnson, V. Meunier and M. Drndić, *ACS Nano*, 2016, **10**, 4134–4142.

60 J. Yang, Y. Wang, M. J. Lagos, V. Manichev, R. Fullon, X. Song, D. Voiry, S. Chakraborty, W. Zhang, P. E. Batson, L. Feldman, T. Gustafsson and M. Chhowalla, *ACS Nano*, 2019, **13**, 9958–9964.

61 P. D. Cunningham, K. M. McCreary, A. T. Hanbicki, M. Currie, B. T. Jonker and L. M. Hayden, *J. Phys. Chem. C*, 2016, **120**, 5819–5826.

62 C. J. Docherty, P. Parkinson, H. J. Joyce, M.-H. Chiu, C.-H. Chen, M.-Y. Lee, L.-J. Li, L. M. Herz and M. B. Johnston, *ACS Nano*, 2014, **8**, 11147–11153.

63 J. Lu, H. Liu and J. Sun, *Nanotechnology*, 2017, **28**, 464001.

64 X. Xing, L. Zhao, Z. Zhang, X. Liu, K. Zhang, Y. Yu, X. Lin, H. Y. Chen, J. Q. Chen, Z. Jin, J. Xu and G. Ma, *J. Phys. Chem. C*, 2017, **121**, 20451–20457.

65 F. Ceballos and H. Zhao, *Advanced Functional Materials*, 2017, **27**, 1604509.

66 J. Lauth, A. Kulkarni, F. C. M. Spoor, N. Renaud, F. C. Grozema, A. J. Houtepen, J. M. Schins, S. Kinge and L. D. A. Siebbeles, *J. Phys. Chem. Lett.*, 2016, **7**, 4191–4196.

67 S. Kar, Y. Su, R. R. Nair and A. K. Sood, *ACS Nano*, 2015, **9**, 12004–12010.

68 F. Ceballos, Q. Cui, M. Z. Bellus and H. Zhao, *Nanoscale*, 2016, **8**, 11681–11688.

69 F. Zhang, Y. Lu, D. S. Schulman, T. Zhang, K. Fujisawa, Z. Lin, Y. Lei, A. L. Elias, S. Das, S. B. Sinnott and M. Terrones, *Science Advances*, 2019, **5**, eaav5003.

70 Y. Lin, X. Ling, L. Yu, S. Huang, A. L. Hsu, Y.-H. Lee, J. Kong, M. S. Dresselhaus and T. Palacios, *Nano Lett.*, 2014, **14**, 5569–5576.

71 P. Hu, J. Ye, X. He, K. Du, K. K. Zhang, X. Wang, Q. Xiong, Z. Liu, H. Jiang and C. Kloc, *Scientific Reports*, , DOI:10.1038/srep24105.